Journal of Magnetic Resonance 211 (2011) 1–10

Contents lists available at ScienceDirect

Journal of Magnetic Resonance

journal homepage: www.elsevier.com/locate/jmr

Time resolved velocity measurements of unsteady systems using spiral imaging

Alexander B. Tayler, Daniel J. Holland, Andrew J. Sederman *, Lynn F. Gladden

Department of Chemical Engineering and Biotechnology, University of Cambridge, Pembroke Street, Cambridge CB2 3RA, United Kingdom

ARTICLE INFO

Article history:
Received 23 November 2010
Revised 10 March 2011
Available online 22 March 2011

Keywords:
Spiral imaging
Phase contrast MRI
Velocity measurement
Turbulent flow
Multiphase flow

ABSTRACT

Spiral imaging has been assessed as a tool for the measurement of spatially and temporally resolved velocity information for unsteady flow systems. Using experiments and simulated acquisitions, we have quantified the flow artefacts associated with spiral imaging. In particular, we found that despite the adverse effect of in-plane flow on the point spread function, for many physical systems the extent of blurring associated with spiral imaging is marginal because flows represented by high spatial Fourier coefficients, which would be those most affected by the distortion of the point spread function, exist at the physical boundaries of the flow and are therefore associated with much smaller velocities than are characteristic of the bulk flow. The necessity for a flow imaging technique which is robust to the accrual of velocity proportionate phase during imaging was demonstrated in an experimental comparison of spiral imaging and echo-planar imaging (EPI) applied to turbulent flow in a pipe. While the measurements acquired using EPI accrued substantial velocity proportionate phase, those acquired using spiral imaging were not significantly affected. High temporal velocity measurements using spiral imaging were demonstrated on turbulent flow in a pipe (image acquisition time 5.4 ms; 91 frames per second), which enabled the transient behaviour of wall instabilities to be captured. Additionally, the technique was applied to a multiphase flow system, where the wakes behind single rising bubbles were characterised. Spiral imaging thus seems an auspicious basis for the measurement of velocity fields for unsteady flow systems.

1. Introduction

Any flowing system which includes some source of instability will demonstrate transient deviations from the time-averaged flow field. These unsteady flow characteristics occur for systems as diverse as turbulent flow in a pipe and multiphase flow. To better understand such transient features it is highly desirable to obtain quantitative, temporally and spatially resolved velocity information. Magnetic Resonance Imaging (MRI) holds several unique advantages over other techniques for the measurement of this type of information, such as particle imaging velocimetry [1] or laser Doppler anemometry [2], including being completely non-invasive (tracers or particles are not required) and being non-optically based (which permits measurements in opaque systems and at any orientation). The principal disadvantage of MRI is that the measurements are slow to acquire relative to the time-scales of the transient flow features under observation. Only the fastest MRI techniques are capable of producing 'snap-shots' of these ephemeral fluid phenomena. In general, this limits acquisitions to single-shot, echo-planar type sequences [3,4]. Even if sufficient time resolution can be achieved, imaging these systems holds additional challenges. In addition to the position dependent ('zeroth moment') phase used for image encoding, some velocity dependent ('first moment') phase may be accrued during imaging, as distinct from velocity proportionate phase which may be purposely applied prior to imaging for velocity encoding. The principal problem for velocity imaging of unsteady systems is that first moment imaging phase cannot be removed by subtraction of an image acquired using an increment in velocity encoding gradient (the conventional approach) because these two images will have been exposed to different velocity fields. For application to fast flows, this can introduce significant image artefacts, and undermines the quantitative nature of phase-contrast velocimetry.

Blipped echo-planar imaging (EPI) [3] is the most commonly used MRI protocol that possesses the temporal resolution sufficient to characterise highly transient flow features. Most commonly, EPI acquires the entire ***k***-space raster in a rectilinear fashion following a single excitation, while using a spin-echo to ensure that off-resonance effects are refocused when the centre of ***k***-space is acquired. EPI, however, traverses the phase direction in a unidirectional manner, which leads to significant first moment weighting by the time the centre of ***k***-space is reached. Tayler et al. [5] proposed an EPI based sequence which somewhat overcame this problem by acquiring both velocity encoded and phase reference data from a single excitation (which were therefore exposed to similar velocities). However this technique does not explicitly compensate for the accrual of first moment imaging

* Corresponding author. Fax: +44 1223334796.
E-mail address: ajs40@cam.ac.uk (A.J. Sederman).

1090-7807/$ - see front matter © 2011 Elsevier Inc. All rights reserved.
doi:10.1016/j.jmr.2011.03.017

phase, and may still be susceptible to flow artefacts. Additionally, it is highly dependent upon favourable relaxation times, and the need to acquire multiple sequential images increases the acquisition time beyond that potentially useful for observation of rapidly changing flow fields. The flow compensation of each individual increment in phase gradient has also been demonstrated [6], however this alteration leads to a significant increase in acquisition time, which undermines the usefulness of the technique for application to highly unsteady systems. Thus, it seems sensible to explore the use of alternative ***k***-space sampling schemes that minimise the accrual of first moment imaging phase. A single-shot technique which traverses ***k***-space in a spiral trajectory [4], which we shall herein refer to as spiral imaging, may hold several advantages in this respect. In particular, the high-power centre of ***k***-space is sampled at the start of the sequence when the transverse plane magnetisation is entirely in phase. Additionally, spiral imaging samples all four quadrants of ***k***-space in an interleaved fashion, which acts to compensate for the accumulation of first moment imaging phase [7].

Spiral imaging has not yet been employed for velocity measurements outside of the medical community. Velocity encoded, single-shot spiral imaging was first implemented by Gatehouse et al. [8], almost simultaneously with Pike et al. [9] who investigated multi-shot interleaved spiral velocimetry. Both sets of researchers verified the measured average flow rate to be quantitative, prior to applying their respective techniques to the *in vivo* measurement of arterial blood flow. Subsequent to these early works, phase contrast spiral imaging has been employed in several medical studies, primarily centred upon applications in cardiology [10–16]. Previous analyses of spiral imaging have noted that the early sampling of the centre of ***k***-space, and the periodic return of all moments of the imaging gradients to zero, rendered the technique highly robust to flow artefacts [7]. Subsequently, however, Butts and Riederer [17] and Gatehouse and Firmin [18] noted that fast (>50 cm s^{-1}) in-plane flows have an adverse effect upon the point spread function (PSF). The PSF is seen to shift in the direction of flow, split into multiple peaks and broaden over several pixels. This behaviour is congruent with the experiments and simulations of Gatehouse et al. [8], who noted that their images fringe and blur respectively in the direction of flow where their flow phantom entered and left the imaging plane, which they identified as being due to the motion of spin isochromats between the start of the sequence, when all low spatial frequencies are sampled, and at its end, when high-resolution information is obtained. Nishimura et al. [19] also simulated acquisitions of spiral imaging in the presence of flow, however they reported that spiral imaging demonstrates minimal flow artefacts even for in-plane velocities in excess of 2 m s^{-1}. This disparity with other studies appears to be due to their simulation of a unidirectional flow phantom of infinite length.

In the present contribution we seek to explore the applicability of spiral imaging towards the quantification of velocity fields for unsteady flow systems. The impact of in-plane flow on the phase image has not been explored to date, and is investigated in the present study using both simulated acquisitions and experiments. With the flow artefacts associated with spiral imaging thereby quantified, we demonstrate the use of spiral imaging for the measurement of velocity fields on some example unsteady flow systems.

2. Simulations

For application to unsteady flow systems, it is important that the accrual of first moment phase during imaging is minimal. It is difficult to demonstrate theoretically that this is the case for spiral imaging because the spiral trajectories used in practice are complex functions of the maximum gradient amplitude and slew rate available [20]. In this section we quantify the extent of flow artefacts for a two dimensional image acquired using a realistic spiral trajectory by simulating the acquisition of spiral images with additional phase accrual originating from the first moment of the imaging gradients. This is possible as the phase accrued while traversing a given gradient waveform is given by:

$$\phi(r,t) = \gamma r \int_0^t g(t)dt + \gamma v \int_0^t tg(t)dt + O(t^3) \quad (1)$$

where γ is the gyromagnetic ratio, r is position in real space and v is the velocity component in the direction of the applied magnetic field gradient. The first term in Eq. (1) represents the zeroth moment phase, which is used for spatial encoding. The second term is the first moment phase, which, if accrued during imaging, gives rise to phase artefacts due to flow. Phase due to higher order terms (e.g. acceleration) may also be accrued, however this is generally small in proportion to the first moment phase. For example, Sederman et al. [21] noted that for single phase flows at a Reynolds number of 5000 (a liquid velocity of 15.1 cm s^{-1} in their system), the maximum fluid acceleration associated with vortex formation was on the order of 40 cm s^{-2}. For an image acquired over 10 ms, the phase accrued due to acceleration is therefore 2.6% of that accrued due to velocity. In the present analysis, phase accrual due to higher moments is considered negligible. The gradient waveform used for all simulations and experiments in this paper was produced by the algorithm of Glover [22] and is shown in Fig. 1. All simulations assumed a spectral width of 357 kHz for a 64 pixel × 64 pixel image with a 5 cm × 5 cm field of view yielding a resolution of 0.78 mm × 0.78 mm. For a given image geometry and velocity field, Eq. (1) was used to generate a first moment phase map for every sampling increment. A set of ***k***-space signals was then generated by application of an inverse non-uniform fast Fourier transform

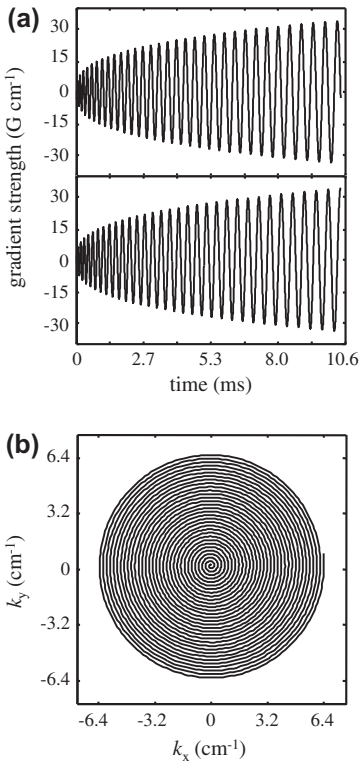

Fig. 1. (a) Spiral gradient waveforms and (b) corresponding ***k***-space trajectory used for simulations and experiments.

[23] to these phase maps and the original modulus image. A simulated signal, complete with flow artefacts, was then constructed by concatenation of the complex data point for each time increment.

To demonstrate the effect of flow upon the modulus of the PSF for spiral imaging, the distortion of a single pixel was simulated for a range of flow rates. In examining these data it is convenient to adopt a dimensionless velocity, defined as:

$$v^* = \frac{v t_i N_p}{\Delta z}, \tag{2}$$

where v is velocity, t_i is the sampling increment, N_p is the number of pixels in one spatial dimension and Δz is the image resolution. It is important to note that, even for a unidirectional flow, the effect upon the PSF for spiral imaging will be two dimensional. This is shown in Fig. 2a for a velocity of 50 cm s^{-1} in the x direction (equivalent to a dimensionless velocity of 1.15×10^{-1}). The PSF is seen to spread in the direction of flow, while also splitting and spreading symmetrically in the perpendicular direction. This splitting is likely responsible for the ringing and fringing of spiral modulus images observed by previous researchers [8]. To quantify the extent of these flow artefacts, the two-dimensional PSF was simulated for a range of velocities, and was then integrated in one direction. These results are shown for the x and y directions in Fig. 2b and c, respectively. The asymmetrical blurring in the flow direction is seen to always be in excess of that in the direction perpendicular to flow, and thus can be solely considered for a conservative estimate of the extent of blurring for spiral imaging of flow. A linear fit to the blurred edge of Fig. 2b yields the relationship:

$$x_b = 2.17 v N_p^2 t_i \tag{3}$$

where x_b is the length over which blurring will take place in the image. Clearly the extent of acceptable blurring depends upon the pixel resolution of an image. This implies that, for images such as those simulated herein (0.78 mm resolution), velocities greater than 3 cm s^{-1} cannot be exceeded without interpixel blurring. For studies in a medical context, however, where resolutions on the order of 5 mm are common, in plane flows of up to 20 cm s^{-1} may be examined with all blurring contained within a single pixel.

To demonstrate the effect of flow artefacts in a system of more general interest, we simulate a more complex geometry and flow field. In particular, a sphere surrounded by a box of fluid is considered as a simulation phantom. In the fluid filled region the velocity is defined as Stokes flow around a sphere, which is given by [24]:

$$u_r = u_\infty \cos\theta \left(1 - \frac{3}{2}\frac{a}{r} + \frac{1}{2}\frac{a^3}{r^3}\right) \tag{4}$$

$$u_\theta = -u_\infty \sin\theta \left(1 - \frac{3}{4}\frac{a}{r} - \frac{1}{4}\frac{a^3}{r^3}\right) \tag{5}$$

where u_r and u_θ are the radial and tangential velocities, respectively. The radius of the sphere is given by a, and u_∞ is the unidirectional

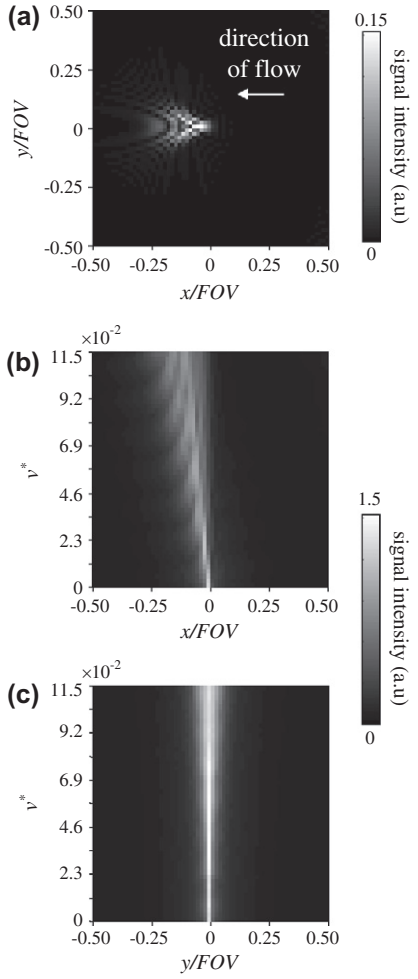

Fig. 2. (a) The effect of flow upon the modulus PSF for spiral imaging for a system with uniform dimensionless velocity, v^* , of 0.115 (spectral width of 357 kHz, 64 × 64 pixel image with a 5 cm × 5 cm field of view, flow velocity of 50 cm s^{-1}). (b) The blurring of the PSF as a function of flow velocity, integrated in the x- direction. (c) The blurring of the PSF as a function of flow velocity, integrated in the y- direction.

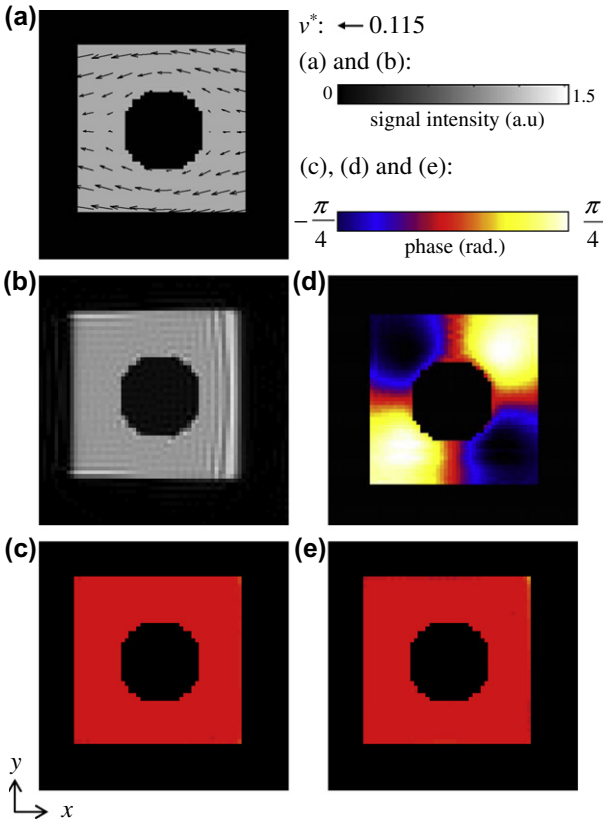

Fig. 3. (a) Input geometry and velocity field for Stokes flow around a 0.8 cm radius sphere in a 3.5 cm × 3.5 cm box of fluid with a far-field dimensionless velocity of 0.115. (b) Modulus and (c) phase images for a simulated acquisition with flow artefacts. (d) Phase map for an image with simulated velocity encoding in the y-direction and (e) difference image for pre- and post-acquisition phase maps. Note that the net shift of images (b), (c) and (e) is caused by the presence of high in-plane velocity in that direction.

velocity of the fluid an infinite distance away from the sphere. Fig. 3a shows the input geometry and velocity field, while (b) and (c) show the resultant modulus and phase images. Data are shown for a 50 cm s^{-1} flow around a 0.8 cm radius sphere with image resolution of 780 μm × 780 μm.

As expected, the substantial in-plane flow present in this simulation has an adverse effect upon the modulus image (b). The whole image is seen to shift in the direction of flow, concurrent with the behaviour of the PSF. A ringing artefact, caused by the oscillations of the PSF, is most clearly visible at the inflowing edge of the simulated phantom where the dispersed signal from the edge adds constructively with the non-displaced signal in the centre. The outflowing edge of the simulated phantom appears blurred, with high-resolution signal from that region displaced off the edge of the simulated region. These artefacts occur over a distance of approximately one quarter of the field of view of the image, in accordance with Eq. (3). The same artefacts are not visible on the fore and aft sides of the sphere because the flow field is derived with a no-slip condition on this boundary. This point has important implications for real systems, where velocities near a boundary are generally significantly decreased from those in the bulk (even for liquid–liquid or gas–liquid interfaces where some slip condition exists). Because the distortion of the PSF is largely limited to signals sampled in the high spatial frequency edges of ***k***-space (i.e. those pixels next to an edge in image space), for systems in which fast flows are limited to regions in the bulk fluid (and are therefore represented by low spatial frequency Fourier coefficients), substantially less distortion of the image should be expected. Additionally, the flow artefacts present on the inflowing and outflowing edges of a sample may be minimised by B_1 heterogeneity in that region, which will result in a gradually attenuated edge to the image. Thus, the practical implementation of spiral imaging (particularly to those systems which lack high resolution flow features) is likely to be more robust to flow than suggested by the PSF.

The effect of flow upon the phase image is demonstrated in Fig. 3c. It is clear that no significant first moment phase accrued during imaging is transmitted through to the phase image. In simulations extending the range of flow rates examined, no significant error or artefact was visible in the phase image for velocities in excess of 2 m s^{-1}. A velocity encoded acquisition was also simulated. This was done by providing an initial phase map in proportion to the *y*-velocity component, shown in Fig. 3d, prior to performing the simulated acquisition. A difference map between the initial and final phase maps is shown in Fig. 3e. It is clear that the ringing and blurring artefacts visible in the modulus image are not present in the phase image. The lack of sharp structures in the flow is representative of many real physical systems, for which velocity images will be very robust to flow artefacts. If high spatial resolution velocity features are to be imaged, the PSF must be considered and blurring will be described by Eq. (3). Within these considerations it is thus evident that spiral imaging is capable of producing quantitative velocity-proportionate phase even in the presence of high in-plane velocities. This is verified experimentally in Section 4. The robustness of the phase image to error suggests that, as long as other sources of phase error are small, spiral imaging does not intrinsically require the subtraction of a reference image. For the removal of phase accrued due to off resonance effects, eddy currents and reconstruction error it has been previously suggested that phase reference data may be generated from stationary fluid included in the imaging region [5,25].

As a final note, if flow artefacts are judged too severe they can be further reduced by the implementation of a variable density spiral sampling trajectory. This is not implemented experimentally in the present paper as we are principally interested in the more robust phase image, however it remains an important consideration as, by adopting an undersampled spiral trajectory, the acquisition time and hence the accrual of first moment imaging phase is greatly decreased. To demonstrate this, Fig. 4 shows a simulation of a 50% undersampled spiral, otherwise identical to the simulations shown in Fig. 3, with the image reconstructed using an iterative compressed sensing procedure [26]. The flow artefacts at the image boundaries in the modulus image shown in Fig. 4b are greatly decreased from those exhibited by the fully sampled spiral given in Fig. 3b. Note that the application of a compressed sensing reconstruction for velocity encoded images has been previously demonstrated by Holland et al. [27].

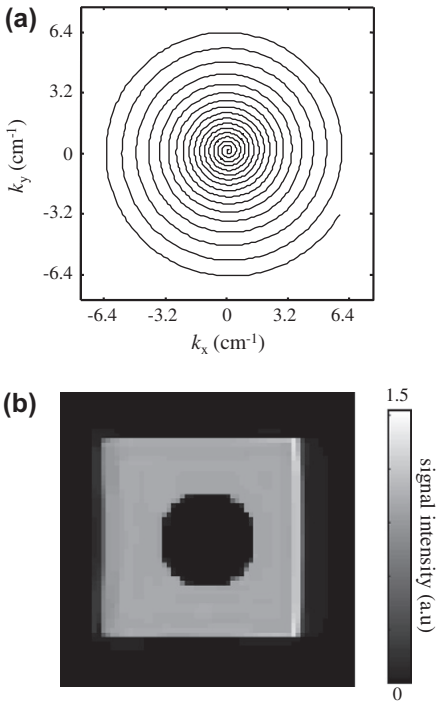

Fig. 4. (a) 50% undersampled spiral image trajectory and (b) modulus of image reconstructed using compressed sensing. Note the flow artefacts are greatly decreased compared to those acquired using a full spiral.

3. Experimental

The pulse sequence for phase contrast spiral imaging is shown in Fig. 5. The slice selection gradient was flow compensated [28], and the velocity encoding lobes (where employed) were applied simultaneously to the slice gradient flow compensation. The image readout gradients followed the maximum gradient limited spiral trajectory, determined as described by Glover [22]. The total acquisition time, AQ, was 12.5 ms obtained at a rate of 55 frames per second (fps) for 64 × 64 pixel images and 5.4 ms at a rate of 91 fps for 32 × 32 pixel images. The liquid phase used in all experiments was distilled water doped with a paramagnetic salt to render the solution magnetic susceptibility matched to air (as described below), and to shorten the relaxation times of the solution (in the present experiments T_1 = 61 ms, T_2 = 50 ms). All images were acquired using a low tip-angle 512 μs Gaussian excitation pulse (5.6° for 32 × 32 pixel images and 11.25° for 64 × 64 pixel images). This low tip-angle permitted rapid repeat acquisitions with minimal relaxation weighting. To verify that no coherent first moment phase was being accrued during imaging, *x*–*z* plane spiral images (where the *z*-coordinate is aligned with the direction of flow) were acquired of laminar flow in a 3 mm tube for comparison with fluid mechanics theory. In a pipe of this diameter laminar

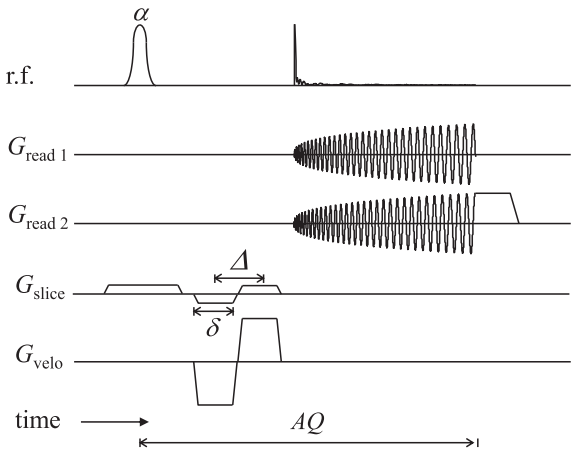

Fig. 5. Pulse sequence for low-angle, snap-shot spiral imaging; $\alpha = 5.6°$ for a 32×32 pixel image, and $\alpha = 11.25°$ for a 64×64 pixel image.

flow is achievable for centreline velocities up to 133 cm s^{-1} (Re = 2000), although to maintain fully developed laminar flow we only examined centreline velocities up to 60 cm s^{-1} (Re = 900). This flow was gravity driven, and controlled using a rotameter and needle valve. In order to quantify the signal attenuation associated with turbulence, spiral images without velocity weighting were acquired of flow in a pipe of diameter 16 mm for the range Re = 500–12,000 (equivalent to cross-sectionally averaged, or superficial, velocities in the range 3.1 cm s^{-1} to 75.0 cm s^{-1}). Non-velocity encoded EPI images were also acquired.

In addition, velocity encoded images were acquired of flows in this range to demonstrate the usefulness of spiral imaging for characterising the transient instabilities associated with turbulent flow. In all flow encoded experiments, reference phase maps were acquired of non-flowing liquid, for the removal of image reconstruction, eddy-current and B_0 inhomogeneity phase errors.

The application of spiral imaging to multiphase flow systems was also explored. In particular, we measured the velocity field around single bubbles as they rose through a stagnant medium. To overcome off-resonance effects associated with imaging two phases of differing magnetic susceptibility, we have matched the magnetic susceptibility of the solution to air. This was achieved using a modified version of the spin-warp pulse sequence [29]. The main alteration to the sequence consists of the addition of a low-bandwidth (150 Hz) plane selective 90° pulse, perpendicular to the imaging slice, prior to each excitation of the imaging sequence. This additional pulse has the effect of saturating a line of constant frequency through the sample. If B_0 is rendered homogeneous for a single phase sample, upon the introduction of a phase interface (i.e. removing half the water from a test-tube) the line of saturated magnetisation will bend to reveal the frequency shift generated by the differing magnetic susceptibility of the two phases. Thus by varying the concentration of paramagnetic salt (dysprosium chloride and gadolinium chloride were used in the present experiments) within the solution until the saturated line is undeflected across the interface, the amount of dopant required for a magnetic susceptibility matched solution was recorded. Surface tension measurements were performed on relatively concentrated (50 mM) solutions of dysprosium chloride and gadolinium chloride using a Dataphysics OCA 15+ goniometer, with surface tensions found to be 71.9 ± 0.3 mN m^{-1} for both solutions (as opposed to 71.4 ± 0.2 mN m^{-1} for undoped water). As the solutions used in the present experiments are always less concentrated than 50 mM, this measurement suggests that the inclusion of such small amounts of salt has a relatively small effect upon the interfacial properties of the solution. While only the dysprosium solution was used in the results reported here, magnetic susceptibility matching data for the gadolinium solution are included for the sake of completeness. Using a magnetic susceptibility matched solution, velocity encoded spiral images were acquired of single bubbles rising in a 20 mm diameter pipe. Bubbles were generated by passing air through a glass capillary of diameter 4 mm using a syringe pump (Harvard Apparatus 22). Phase reference images were acquired of uniform, stationary liquid for the isolation of phase imparted during velocity encoding. Note that this procedure can only be applied to a magnetic susceptibility matched two-phase system, as otherwise B_0 inhomogeneity phase shifts will occur at the phase interface.

All measurements were performed on a Bruker AV-400 spectrometer, operating at a ^{1}H resonance frequency of 400.25 MHz. A three-axis, shielded gradient system with a maximum strength of 146 G cm^{-1} was used for zeroth and first gradient moment encoding, and a 25 mm diameter birdcage r.f. coil was used for excitation and signal reception. For all experiments involving velocity encoding, the flow encoding time (δ) was 416 μs, and the flow contrast time (Δ) 516 μs. The velocity was determined from the image phase by the relation:

$$v = \frac{\arg(\rho)}{2\pi A \gamma \delta \Delta} \tag{6}$$

where ρ is the complex image, A is the velocity encoding gradient strength, selected in order to maximise a velocity dependent phase shift with a 2π window. The $\boldsymbol{k}$-space trajectory followed during acquisition was measured using a modified version of the technique of Duyn et al. [30], which used a volume selective excitation to overcome errors in the phase measurement associated with B_0 heterogeneity (which was particularly problematic in the z-direction). To correct for the disparity in the sampling density of $\boldsymbol{k}$-space associated with spiral imaging, all acquired data were weighted using a Voronoi sampling-density compensation function [31] prior to image reconstruction using a non-uniform fast Fourier transform [23].

4. Results

The simulations provided in the previous section predicted minimal error in the phase image due to in-plane flow for spiral imaging. We presently validate this hypothesis experimentally. Additionally, we explore the degree to which spiral imaging is afflicted by signal attenuation caused by shear, which is another significant flow artefact commonly associated with echo-planar type sequences. The error in modulus and phase images acquired using EPI and spiral imaging are then compared. Finally, we demonstrate some examples of spiral imaging based velocity measurements on high-shear, unsteady flow systems.

4.1. Error in the phase image

The simulations suggest that the accrual of first moment imaging phase should not introduce substantial errors into the phase image. We have validated this assertion experimentally by acquiring longitudinal plane spiral images, with and without velocity encoding, for laminar flow in a pipe. By using a small diameter pipe (3 mm) we were able to maintain laminar flow up to a centreline velocity of 60 cm s^{-1} (Re = 900). Fig. 6 shows both a phase profile extracted from a non-velocity encoded image and a comparison of a velocity profile at this flowrate with the theoretical result of Hagen-Poiseuille. That no significant phase shift is present in the former, while good agreement between experiment and theory is evident in the latter, reinforces that no significant systematic error due to the imaging gradients is present in the phase image. A small phase offset of approximately 0.05 radians was noted in the

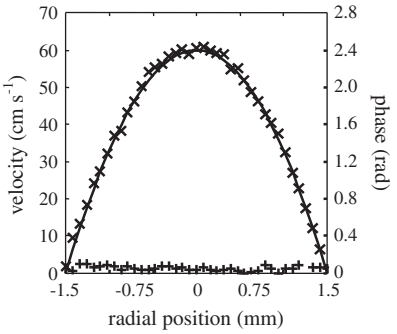

Fig. 6. Velocity profile (or phase) obtained from a phase image for a system with high in-plane flow with (×) and without (+) flow encoding gradients. The velocity profile expected from fluid mechanics theory for laminar flow is also shown (line). These images were obtained with a 5 mm field of view and a resolution of 78 μm. The lack of phase in the image without flow encoding gradients and the good agreement between theory and experiment when the flow encoding gradients are turned on suggests that no significant velocity encoding is occurring due to the imaging gradients and that flow measurement is quantitative.

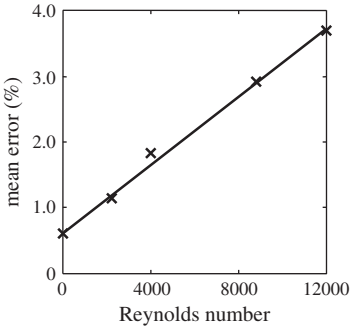

Fig. 7. Error in the signal modulus as a function of Reynolds number for spiral imaging of single phase flow in a pipe of diameter 16 mm. A linear trend fitted to the data is shown to guide the eye.

non-velocity encoded profile, the origin of this is most likely to be phase accrual due to off-resonance effects. The noise level in the profile corresponds to a measurement error of approximately 2%.

4.2. Signal attenuation due to high-shear

It is well known that turbulent flow in the presence of a magnetic field gradient (either due to B_0 inhomogeneity [32] or applied gradients [33]) leads to localised signal attenuation. This occurs due to the presence of substantially different velocities in close proximity to each other, which when combined with some degree of first moment phase accrual, leads to different phases mixing within individual voxels. These phases add destructively to attenuate the net signal for a particular voxel. This is particularly problematic for highly unsteady systems, such as turbulent flow in a pipe. In this section we seek to quantify the signal attenuation due to turbulence. In doing this, non-velocity encoded cross-sectional plane images were acquired of turbulent flow in a 16 mm diameter pipe up to a Reynolds number of 12,000. By comparing the modulus of these images with a reference image of stagnant liquid, a measurement of signal attenuation as a function of Reynolds number was extracted. These data are shown in Fig. 7. The mean error present at Re = 0 represents a measurement error due to noise of 0.6%. It is evident that shear induced signal attenuation is insubstantial for spiral imaging, with a mean error of approximately 3.5% for a Reynolds number of 12,000. The reason this error is so small is likely due to the centre of $\boldsymbol{k}$-space (and hence the bulk of the signal intensity) being acquired at the start of the sequence, when little or no first moment imaging phase exists. Thus spiral imaging may prove useful for obtaining velocimetric information in high shear systems (where comparable EPI based techniques are heavily attenuated), and also for measurements which require that the signal modulus remain quantitative in the presence of shear (see for example Tayler et al. [34]).

4.3. Comparison of spiral imaging and EPI in application to unsteady flow systems

Given the minor accrual of first moment imaging phase, spiral imaging seems an auspicious basis for snap-shot velocity imaging of unsteady flow. Spiral imaging is advantageous compared to EPI in this application, as it removes the systematic error in the phase image associated with the imaging gradients. This is demonstrated in Fig. 8, which shows a comparison of non-velocity encoded blipped-EPI and spiral images of turbulent flow in a pipe at a Reynolds number of 8800. Both modulus and phase images are shown. It is clear that while significant shear attenuation is present in the modulus EPI image (mean error of 24.8%), the spiral image is much more robust (mean error of 2.8%; in accordance with Fig. 7). Furthermore, significant coherent structures exist in the EPI phase image, reflecting that flow encoding has occurred in one direction due to the imaging gradients. Conversely, no phase exists in the spiral image, which reflects the robustness of the technique to flow. The degree of error present in the EPI images is a function of the imaging gradient strength used and transverse plane velocity components. Of course, EPI may still be appropriate for application to unsteady flow where the resolution or in-plane velocities are lower than those examined herein.

4.4. Velocity imaging of unsteady flow systems using spiral imaging

The present implementation of spiral imaging acquires data directly from an FID, significantly decreasing the acquisition time (relative to spin-echo based imaging sequences) and allowing smaller tip angles to be used, and thus permitting rapid repeat excitations without relaxation weighting. This allows some highly transient flow features to be imaged for the first time. Consider, for example, Fig. 9, which shows a number of time sequential velocity images of unsteady flow in a pipe (Re = 4500). Attention is drawn to the wall region, where an instability is visible extending from the wall; snaking to and fro in the main body of the fluid. The acquisition rate of these images (91 fps) is just sufficient to characterise this highly transient fluid phenomenon.

An interesting juxtaposition exists between these data and those of Sederman et al. [21], who acquired multiple sequential images of turbulent flow using EPI from the same excitation. Whereas they noted the turbulent structures to be relatively constant over an 80 ms period, from the present images it is clear that the flow field changes substantially over the course of 10 ms. The reason for this disparity is that the present images (which were each acquired from a fresh excitation) show an Eulerian velocity represented in an Eulerian frame of reference, whereas those acquired by Sederman et al. depict an Eulerian velocity however now in the Lagrangian frame. The difference between these two measurements lies in the way they observe changes to the flow field; while the sequence of velocity measurements acquired using spiral imaging are acquired at a fixed spatial location, the measurements of Sederman et al. were acquired from repeatedly refocused magnetisation and therefore yield signal from a mobile packet of fluid. To demonstrate this difference, consider Fig. 10, which shows longitudinal plane velocity images of the turbulent flow system examined above. It is clear from these images that the turbulent features (that is the regions of fast and slow moving fluid

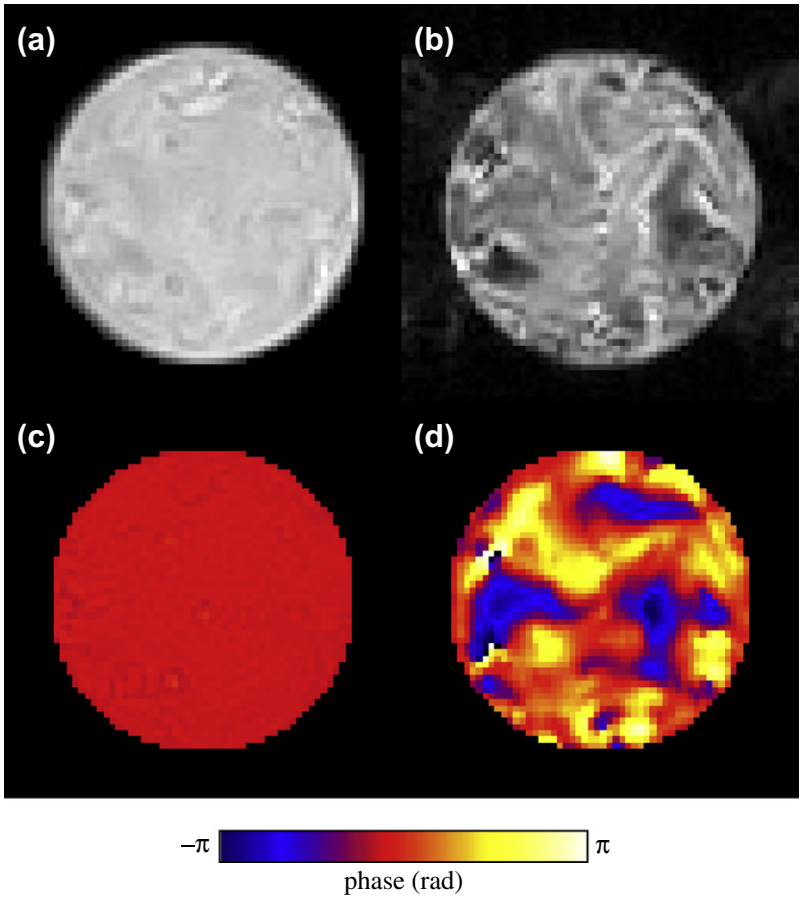

Fig. 8. Comparison of non-velocity encoded spiral and EPI images of turbulent pipe flow at a Reynolds number of 8800 in a pipe of inside diameter 16 mm. Modulus images are shown for (a) spiral imaging and (b) EPI. Phase images are shown for (c) spiral imaging and (d) EPI. The in-plane shear and velocity result in attenuation of the signal and the accrual of significant phase shifts during EPI, but not spiral imaging. Note that the slice selection gradients were velocity compensated for both imaging techniques. The spatial resolution is 313 μm × 313 μm for a field of view of 20 mm × 20 mm.

immediately adjacent to each other) are transmitted along the pipe as coherent and relatively slowly evolving structures. These structures are seen to move along the pipe at approximately the superficial velocity of the fluid, and in this context are stable for approximately 80 ms, consistent with the findings of Sederman et al. [21]. Fig. 10 also demonstrates the successful application of spiral imaging for velocity measurements on a system which contains high in-plane flows. According to Eq. (3), blurring of the PSF can be expected over 2.8 mm (approximately 3 pixels) in this image in the direction of flow.

4.5. Application of spiral imaging to multiphase flow systems

One limitation of any long read-out, single-shot sequence is a susceptibility to off-resonance effects. In this respect, spiral imaging is perhaps even less robust than EPI. This is because while B_0 inhomogeneities tend to distort EPI images in a coherent manner, spiral imaging suffers from localised signal attenuation. Artefacts due to B_0 inhomogeneity are normally overcome in spiral imaging by resorting to a multi-shot spiral (with the equivalently shortened acquisition period [20]). Clearly for our present application it is necessary to preserve the time resolution associated with a single shot technique. Overcoming B_0 inhomogeneities is a particular challenge for the application of spiral imaging to multiphase flow systems, which tend to be composed of materials of differing magnetic susceptibility, with effective shimming made difficult or impossible by the complex geometries and the dynamic nature of the phase interfaces.

Here we examine the application of spiral imaging to gas–liquid flow systems, although the techniques described herein are equally applicable to other forms of multiphase flow systems. To eliminate off-resonant effects due to magnetic susceptibility differences we have doped the aqueous phase with a paramagnetic salt such that the magnetic susceptibility of the liquid is identical to that of the gaseous phase. To this end, Fig. 11 was produced using the magnetic susceptibility matching procedure described in the experimental section, as applied to both dysprosium chloride and gadolinium chloride solutions. Dysprosium ions are seen to have a stronger effect upon the magnetic susceptibility than gadolinium, with a magnetic susceptibility matched solution being reached at a concentration of 16.8 mM, compared with 27.7 mM for the gadolinium. A magnetic susceptibility matched dysprosium solution was chosen for the present experiments because of its favourable relaxation properties for single-shot measurements (T_1 = 61 ms, T_2 = 50 ms). Gadolinium has a much stronger influence upon the relaxation rates, which may render gadolinium doped solutions more appropriate for use with multi-shot, short readout sequences.

Velocity encoded spiral images were acquired of single bubbles rising through this solution in a 20 mm diameter pipe. Eight sequential frames, acquired at a rate of 55 fps, of an example bubble rising through the imaging region are shown in Fig. 12. The approximate position and shape of the bubble (identified from the modulus images) is represented by the filled ellipse in each image. An air bubble of spherically equivalent diameter 2.5 mm can be expected to rise at a rate of approximately 20 cm s^{-1} in surfactant free water and have velocities of approximately double this

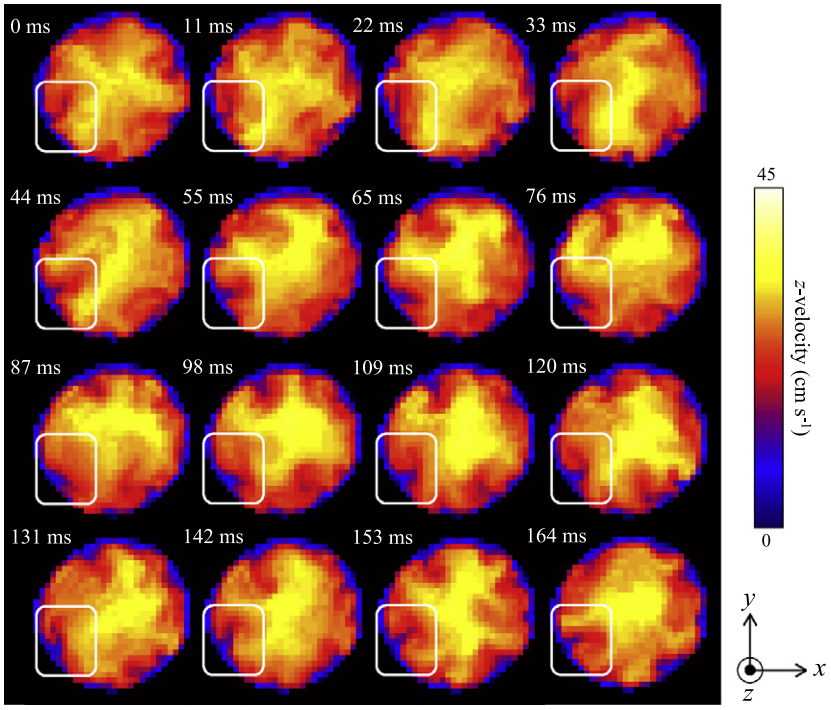

Fig. 9. Cross-sectional maps of the z-velocity of unsteady flow acquired using spiral imaging (Re = 4500). The transient behaviour of a wall instability is highlighted. The acquisition rate of these images is 91 fps. The times shown on the images refer to the start of the acquisition. The spatial resolution is 625 μm × 625 μm for a field of view of 20 mm × 20 mm. A video displaying these data played back at a tenth of real time is available as Supplementary data online.

value in the bubble's wake [35]. From the modulus images, we measured the rise rate of the bubble to be 21.1 ± 0.7 cm s^{-1}, with velocities in the range −39.4 cm s^{-1} to 39.4 cm s^{-1} in the bubble's wake, which is consistent with the theory. The structure of the wake is clear in these images, as is the liquid displaced downward at the sides of the bubble (indicated by the negative velocities). Also visible are periodic vortex shedding events, wherein the wake of the bubble detaches and a region of liquid flows upward independently until its momentum has been dispersed throughout the fluid. It is known that these wake shedding events occur at a frequency of 12 Hz independent of bubble size [36]. Each bubble was present in the imaging region for 150 ms, which is long enough for one complete cycle of wake shedding to occur. The frequency of wake shedding was observed to be constant within the temporal resolution of the technique (±1.1 Hz) for ten consecutive bubbles, and occurs at a rate of 11.0 Hz, which is consistent with the expected frequency. According to Eq. (3), the PSF for these images may be distorted by a maximum of 9.8 mm, however as the highest velocities in the system are limited to regions represented by low spatial frequency Fourier coefficients, and as the velocity field does not contain high resolution features, the effect of this blurring is largely mitigated. These velocity maps illustrate the great potential of spiral imaging for the characterisation of multiphase flow systems.

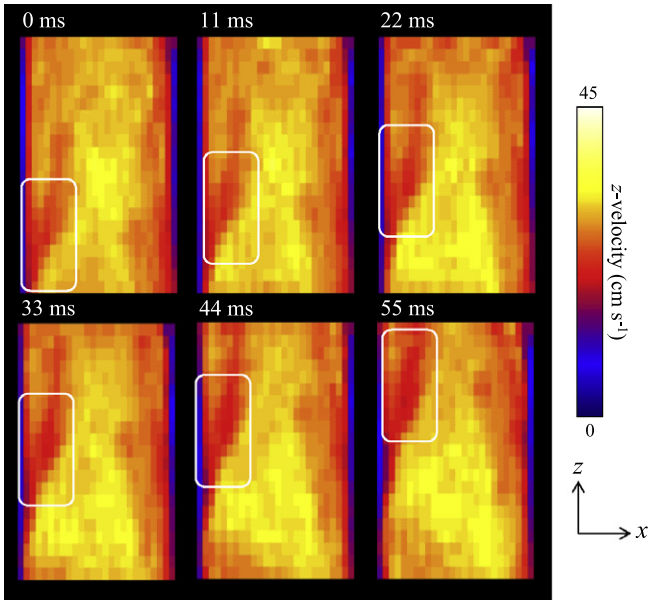

Fig. 10. Longitudinal maps of the z-velocity of fully developed unsteady flow acquired using spiral imaging (Re = 4500). A slowly evolving turbulent structure is highlighted by the rounded white box. The acquisition rate of these images is 91 fps. The times shown on the images refer to the start of the acquisition. The spatial resolution is 625 μm × 984 μm for a field of view of 20 mm × 31.5 mm. A video displaying these data played back at a tenth of real time is available as Supplementary data online.

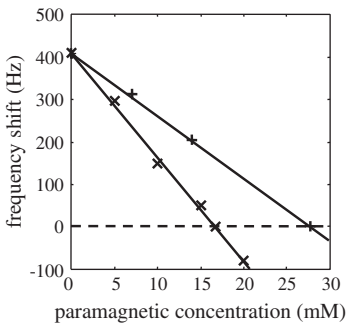

Fig. 11. Frequency shift across a phase interface due to magnetic susceptibility difference for (×) dysprosium chloride and (+) gadolinium chloride solutions with air.

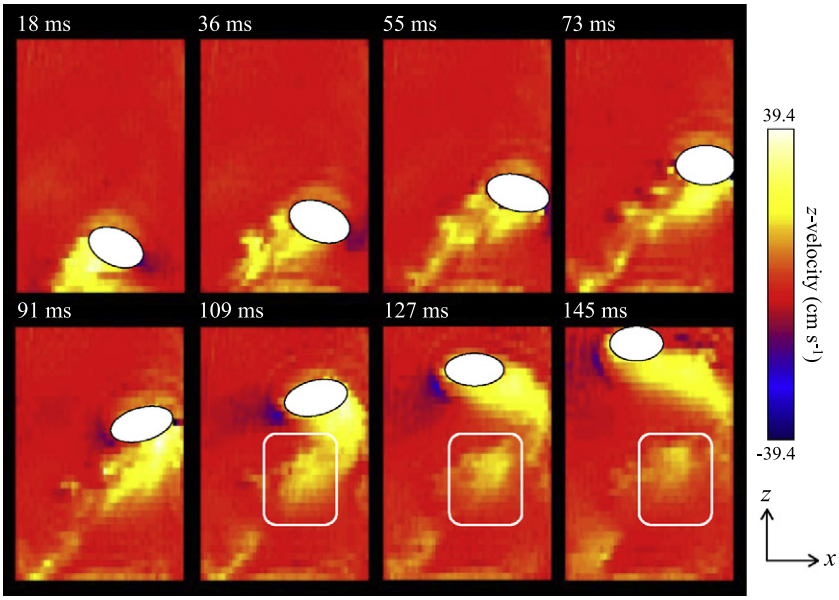

Fig. 12. Longitudinal maps of the z-velocity for a single bubble rising through a magnetic susceptibility matched solution of dysprosium chloride. The approximate locations of the bubble are highlighted by the filled white ellipses. A vortex shedding event is highlighted by the rounded white box. The acquisition rate of these data is 55 fps. The times shown on the images refer to the start of the acquisition. The spatial resolution is 390 μm × 586 μm for a field of view of 25 mm × 37.5 mm. A video displaying these data played back at a fifth of real time is available as Supplementary data online.

5. Conclusions

Spiral imaging has been assessed as a technique for the quantification of time-resolved velocity fields for unsteady flow systems. Using simulated acquisitions we have quantified the extent of the distortion to the PSF for spiral imaging due to flow, and noted that the impact of this artefact is minimal for many physical systems. This is because flows near an edge in image space (i.e. corresponding to heavily first moment weighted high-frequency Fourier coefficients) are boundary affected and thus are often significantly decreased from the bulk fluid velocity. We have also quantified the shear induced, localised attenuation in the modulus image, and found errors to be less than 3.5% for flows up to a Reynolds number of 12,000 for single phase flow in a pipe. These errors are likely so small due to the early sampling of the centre of $\boldsymbol{k}$-space associated with spiral imaging. The acquisition of velocity fields using spiral imaging was then demonstrated on some example unsteady flow systems. Non-velocity encoded images acquired using both EPI and spiral imaging of turbulent pipe flow were compared, with significant errors in the modulus and velocity proportionate phase present in the EPI images. Conversely the spiral images were relatively robust in both the modulus and phase images. This demonstrates the superiority of spiral imaging for the measurement of quantitative velocity fields of unsteady systems. Turbulent flow in a pipe was imaged at a time resolution of 91 fps, and the behaviour of highly transient wall instabilities were captured by MRI for the first time. The sequence was also demonstrated by imaging the wake around rising single bubbles, and such flow features as vortex shedding were clearly visible. Spiral imaging was thus shown to be a highly promising basis for the acquisition of temporally and spatially resolved velocity information for unsteady systems, and may prove particularly useful for the characterisation of multiphase flows.

Acknowledgments

The authors wish to express their gratitude to the EPSRC for support under the grant EP/F047991/1. DJH and AJS would also like to thank Microsoft Research, and ABT would like to thank the Cambridge Commonwealth Trust and Trinity College, Cambridge. Finally, they wish to thank Bruce Lee at the University of Newcastle, Australia, for performing the surface tension measurements.

Appendix A. Supplementary material

Supplementary data associated with this article can be found, in the online version, at doi:10.1016/j.jmr.2011.03.017.

References

[1] R.J. Adrian, Particle-imaging techniques for experimental fluid mechanics, Annu. Rev. Fluid Mech. 23 (1991) 261–304.
[2] P. Buchhave, W.K. George, J.L. Lumley, The measurement of turbulence with the laser-Doppler anemometer, Annu. Rev. Fluid Mech. 11 (1979) 443–503.
[3] P. Mansfield, Multi-planar image formation using NMR spin echoes, J. Phys. C 10 (1977) L55–L58.
[4] C.B. Ahn, J.H. Kim, Z.H. Cho, High-speed spiral scan echo planar NMR imaging – I, IEEE T. Med. Imag. 5 (1986) 2–5.
[5] A.B. Tayler, A.J. Sederman, B. Newling, M.D. Mantle, L.F. Gladden, 'Snap-shot' velocity vector mapping using echo-planar imaging, J. Magn. Reson. 204 (2010) 266–272.
[6] J.L. Duerk, O.P. Simonetti, Theoretical aspects of motion sensitivity and compensation in echo-planar imaging, J. Magn. Reson. Imag. 1 (1991) 643–650.
[7] C.H. Meyer, B.S. Hu, D.G. Nishimura, A. Macovski, Fast spiral coronary artery imaging, Magn. Reson. Med. 28 (1992) 202–213.
[8] P.D. Gatehouse, D.N. Firmin, S. Collins, D.B. Longmore, Real time blood flow imaging by spiral scan phase velocity mapping, Magn. Reson. Med. 31 (1994) 504–512.
[9] G.B. Pike, C.H. Meyer, T.J. Brosnan, N.J. Pelc, Magnetic resonance velocity imaging using a fast spiral phase contrast sequence, Magn. Reson. Med. 32 (1994) 476–483.
[10] K.S. Nayak, J.M. Pauly, A.B. Kerr, B.S. Hu, D.G. Nishimura, Real-time color flow MRI, Magn. Reson. Med. 43 (2000) 251–258.
[11] J.B. Park, E.W. Olcott, D.G. Nishimura, Rapid measurement of time-averaged blood flow using ungated spiral phase-contrast, Magn. Reson. Med. 49 (2003) 322–328.
[12] K.S. Nayak, B.S. Hu, D.G. Nishimura, Rapid quantitation of high-speed jets, Magn. Reson. Med. 50 (2003) 366–372.
[13] J.B. Park, J.M. Santos, B.A. Hargreaves, K.S. Nayak, G. Sommer, B.S. Hu, D.G. Nishimura, Rapid measurement of renal artery blood flow with ungated spiral phase-contrast MRI, J. Magn. Reson. Imag. 21 (2005) 590–595.
[14] J.B. Park, B.S. Hu, S.M. Conolly, K.S. Nayak, D.G. Nishimura, Rapid cardiac-output measurement with ungated spiral phase contrast, Magn. Reson. Med. 56 (2006) 432–438.

[15] J.L.A. Carvalho, K.S. Nayak, Rapid quantitation of cardiovascular flow using slice-selective Fourier velocity encoding with spiral readouts, Magn. Reson. Med. 57 (2007) 639–646.
[16] A. Harloff, F. Albrecht, J. Spreer, A.F. Stalder, J. Block, A. Frydrychowicz, J. Schöllhorn, A. Hetzel, M. Schumacher, J. Hennig, M. Markl, 3D blood flow characteristics in the carotid artery bifurcation assessed by flow-sensitive 4D MRI at 3T, Magn. Reson. Med. 61 (2009) 65–74.
[17] K. Butts, S.J. Riederer, Analysis of flow effects in echo-planar imaging, J. Magn. Reson. Imag. 2 (1992) 285–293.
[18] P.D. Gatehouse, D.N. Firmin, Flow distortion and signal loss in spiral imaging, Magn. Reson. Med. 41 (1999) 1023–1031.
[19] D.G. Nishimura, P. Irarrazabal, C.H. Meyer, A velocity *k*-space analysis of flow effects in echo-planar and spiral imaging, Magn. Reson. Med. 33 (1995) 549–556.
[20] K.T. Block, J. Frahm, Spiral imaging: a critical appraisal, J. Magn. Reson. Imag. 21 (2005) 657–668.
[21] A.J. Sederman, M.D. Mantle, C. Buckley, L.F. Gladden, MRI technique for measurement of velocity vectors, acceleration, and autocorrelation functions in turbulent flow, J. Magn. Reson. 166 (2004) 182–189.
[22] G.H. Glover, Simple analytic spiral *k*-space algorithm, Magn. Reson. Med. 42 (1999) 412–415.
[23] J.A. Fessler, B.P. Sutton, Nonuniform fast Fourier transform using min–max interpolation, IEEE Trans. Signal Process. 51 (2003) 560–574.
[24] H. Lamb, Hydrodynamics, Cambridge University Press, Cambridge, 1895.
[25] L.C. Man, J.M. Pauly, D.G. Nishimura, A. Macovski, Nonsubtractive spiral phase contrast velocity imaging, Magn. Reson. Med. 42 (1999) 704–713.
[26] M. Lustig, D.L. Donoho, J.M. Pauly, Sparse MRI: the application of compressed sensing for rapid MR imaging, Magn. Reson. Med. 58 (2007) 1182–1195.
[27] D.J. Holland, D.M. Malioutov, A. Blake, A.J. Sederman, L.F. Gladden, Reducing data acquisition times in phase-encoded velocity imaging using compressed sensing, J. Magn. Reson. 203 (2010) 236–246.
[28] J.M. Pope, S. Yao, Quantitative NMR imaging of flow, Concept. Magn. Reson. 5 (1993) 281–302.
[29] W.A. Edelstein, J.M.S. Hutchison, G. Johnson, T. Redpath, Spin warp NMR imaging and applications to human whole-body imaging, Phys. Med. Biol. 25 (1980) 751–756.
[30] J.H. Duyn, Y. Yang, J.A. Frank, J.W. van der Veen, Simple correction method for *k*-space trajectory deviations in MRI, J. Magn. Reson. 132 (1998) 150–153.
[31] F. Aurenhammer, Voronoi diagrams – a survey of a fundamental geometric data structure, Comput. Surv. 23 (1991) 345–405.
[32] P.G. De Gennes, Theory of spin echoes in a turbulent fluid, Phys. Lett. A 29 (1969) 20–21.
[33] K. Fukuda, A. Hirai, A pulsed NMR study on the flow of fluid, J. Phys. Soc. Jpn. 47 (1979) 1999–2006.
[34] A.B. Tayler, D.J. Holland, A.J. Sederman, L.F. Gladden, The quantification of bubble size distributions using ultra-fast MRI, in: Proc. 7th Int. Conf. Multiphase Flow, 2010.
[35] R. Clift, J.R. Grace, M.E. Weber, Bubbles, Drops, and Particles, Academic press, New York, 1978.
[36] K. Lunde, R.J. Perkins, Shape oscillations of rising bubbles, Appl. Sci. Res. 58 (1998) 387–408.